ADVANCED MATERIALS INTERFACES

www.advmatinterfaces.de

Vertical Phase Separation for Highly Efficient Organic Solar Cells Incorporating Conjugated-Polyelectrolytes

*Yong Woon Han, Jun Young Choi, Ye Jin Lee, Eui Jin Ko, Min Hee Choi, Il Soon Suh, and Doo Kyung Moon**

Hybrid organic solar cells are made through a simple one-pot coating process with conjugated polyelectrolytes (CPEs), poly[9,9-bis(4′-sulfonatobutyl)fluorenealt-thiophene-doped (PFT-D). The hybrid active layer incorporated with PFT-D shows vertical phase separation by self-assembled properties of PFT-D, which result from a molecular dipole between the conjugated backbone and the side chain. The hybrid active layer with PFT-D shows that homogeneous morphology, surface potential properties, and hydrophobic surface properties favor for enhancing photovoltaic performance. These results are identified by contact angle characteristics, X-ray photoelectron spectroscopy (XPS) profiling, and X-ray diffraction (XRD), atomic force measurement (AFM), and electrostatic force measurement (EFM) analyses. With fullerene based hybrid active layer, the power conversion efficiency (PCE) reaches to 8.7% with the enhanced short-circuit current density (J_{SC}), open-circuit voltage (V_{OC}), and fill factor (FF). The hybrid device with PFT-D has a higher stability with a lower reduction ratio of 5.74% compared with only bulk-heterojunction device (with reduction rate of 30.15%) and incorporating poly(3,4-ethylene dioxythiophene)-poly(styrene sulfonate) (PEDOT:PSS) device (with reduction rate of 10.84%). These results are also found in nonfullerene based system (PCE of 10.8%) and other conjugated polyelectrolytes system (PCE of 8.4%). These results have the potential of significantly contributing to the upsizing and commercialization of organic solar cells.

1. Introduction

There have been many studies on organic solar cells (OSCs) that have been based on polymer semiconductors because OSCs can be applied to various fields due to their many advantages, such as high performance, low cost, flexibility, and potential for modulation. Recently, the research on OSCs has been focused on materials with high-performance organic donors and acceptors (fullerene and nonfullerene) and device structure research, such as ternary structure and tandem structure. These studies have contributed to developing high-performance OSCs with excellent power conversion efficiency (PCE) over 14% in single cells and 17.3% in tandem structure cells.[1–10]

OSCs are based on an active layer that has a bulk-heterojunction (BHJ) structure that consists of an organic donor and acceptor, and OSCs generate excitons within the range of their optical properties. Additionally, OSCs show photovoltaic properties via the process of charge disassociation and charge transport.[11,12] Due to the limitation of the optical properties of organic donors and acceptors, carrier mobility and carrier balance are critical factors that determine the performance of OSCs.[13–16]

Therefore, photogenerated carriers that have been generated in a BHJ have the disadvantage of exhibiting a lower mobility compared with inorganic semiconductor-based solar cells because of the organic semiconductor's inherent properties, such as monomolecular recombination and bimolecular recombination.[17–19]

Additionally, certain of these photogenerated carriers return to the ground state through monomolecular trap-assisted recombination,[20–22] interfacial recombination,[23–25] and surface trap-assisted recombination,[26] and the carriers subsequently weaken the device performance because the reduction of current and internal potential occurs via a nonradiative relaxation process.[27,28] Therefore, it is necessary to enhance the carrier transport properties to improve the performance of OSCs.

Recent research has reported important device structure modifications to improve the carrier transport properties of OSCs. Specifically, the carrier mobility can be increased by introducing a buffer layer through enhancing carrier transport, and the device performance can be enhanced by reducing the recombination.

Y. W. Han, J. Y. Choi, Y. J. Lee, E. J. Ko, Prof. I. S. Suh, Prof. D. K. Moon
Nano and Information Materials Lab. (NIMs Lab.)
Department of Chemical Engineering
Konkuk University
120 Neungdong-ro, Gwangjin-gu, Seoul 05029, Republic of Korea
E-mail: dkmoon@konkuk.ac.kr

Dr. M. H. Choi
Progressive Technology Research Group
KOLON Central Research Park
30, Mabuk-ro 154 beon-gil, Giheung-gu, Yongin-si 16910
Gyeonggi-do, Republic of Korea

The ORCID identification number(s) for the author(s) of this article can be found under https://doi.org/10.1002/admi.201801396.

DOI: 10.1002/admi.201801396

Huang and co-workers developed a device of conventional structure by using electron transport layers (ETLs). To develop the device, they introduced an organic buffer layer, poly[(9,9-bis(6′-((N,N-diethyl)-N-ethyl ammonium)-hexyl)-2,7-fluorene)-alt-1,4-diphenylsulfide]dibromide, as the poly[(9,9-bis-(3′-(N,N-dimethylamino)propyl)-2,7-fluorene)-alt-2,7-(9,9-dioctylfluorene)] (PFN) series that was introduced via a solution process as an ETL. They reported that they attained a high PCE of 9.45% by enhancing the carrier mobility and lowering the recombination, regardless of the thickness of the ETLs.[29]

Next, Lee et al. introduced conjugated polyelectrolytes (CPEs), the poly(9,9-bis(4′-sulfonatobutyl)fluorene-alt-co-1,4-phenylene)] (PFT) series, as hole transport layers (HTLs). They observed a work function change phenomenon for the indium tin oxide (ITO) electrode of the device. They were able to obtain an excellent PCE of 9.03% by controlling the work function change.[30]

Generally, poly(3,4-ethylene dioxythiophene)-poly(styrene sulfonate) (PEDOT:PSS), which is a buffer layer introduced into OSCs, plays an important role in improving hole mobility because of its advantage of transparency and high conductivity. It, however, has the disadvantage of diminishing the device stability due to its hygroscopic properties and inherent acidic properties.[31,32] Several studies have reported that inorganic materials, such as MoO_3,[33,34] WO_3,[35] NiO,[36] and CuSCN,[37,38] are candidate that may replace PEDOT:PSS to overcome the disadvantages of PEDOT:PSS. However, these materials also have some problems, such as thermal treatment and interfacial mixing.

Recently, researchers have paid attention to CPEs as HTLs that can replace PEDOT:PSS because they have neutral properties, outstanding solubility, and high mobility resulting from the molecular dipole.[30,39–43] Heeger and co-workers reported that they were able to weaken the series resistance (R_S) by introducing CPE-K into HTLs of OSCs by using a spin-coating method, which is a solution process. The PCE of 8.2% was higher when introducing CPE-K compared to that when introducing PEDOT:PSS.[39] Chen and co-workers also reported that they obtained a high PCE of 9.6% in OSCs by developing two types of CPEs poly[2,6-dibromo-(4,4-bis-potassium butanylsulfonate-4H-cyclopenta-[2,1-b;3,4-b']-dithiophene-alt-2,5-thiophene)] (PCPDT-T) and poly[2,6-dibromo-(4,4-bis-potassium butanylsulfonate-4H-cyclopenta-[2,1-b;3,4-b']-dithiophene-alt-2,2'-bithiophene)] (PCPDT-2T)) as new HTLs.[40]

However, the technique of introducing a buffer layer to increase the carrier mobility and to decrease the carrier recombination may instead weaken the device performance and long-term stability because it causes issues with an additional process, such as an increased cost and interfacial mixing problems between the BHJ and electrode. Previous work in our group indicated that the PCE and stability are enhanced by developing CPEs that replace PEDOT:PSS with HTLs.[41]

Recently, Hao and co-workers found an improved PCE from 9.6% to 11.0% by using a ternary BHJ device that adopted the third component in a binary BHJ. This result confirms that vertical phase separation, which has the advantage of charge transport in BHJ by introducing the third component, was formed.[44] Lee and co-workers induced vertical phase separation by using the difference in surface energy properties in a device that was made via a one-step coating process with the introduction of self-assembly interfacial materials. As a result, they achieved a PCE of 6.1%.[45]

In conclusion, developing a device with a high performance and stability should be possible with a simple process if: 1) CPEs with excellent performance and stability are used, 2) CPEs can be introduced via a simple coating process in the BHJ through hybridization without an additional coating process for the HTLs, and 3) there is control of the vertical phase within the BHJ.

In this paper, we report a method to fabricate a device simply by using a BHJ active layer coating after inducing self-assembled order based on the molecular dipole properties of CPEs by incorporating them into the BHJ active layer. We formed a one-pot hybrid active layer by introducing CPEs of PFT-D into a BHJ active layer that uses poly({4,8-bis[(2-ethylhexyl)oxy]benzo[1,2-*b*:4,5-b']dithiophene-2,6-diyl}{3-fluoro-2-[(2-ethylhexyl)carbonyl]thieno[3,4-*b*]thiophenediyl}) (PTB7), poly[(2,6-(4,8-bis(5-(2-ethylhexyl)thiophen-2-yl)-benzo[1,2-b:4,5-b']dithiophene))-alt-(5,5-(1',3'-di-2-thienyl-5',7'-bis(2-ethylhexyl) benzo[1',2'-c:4',5'-c']dithiophene-4,8-dione))]) (PBDB-T) as a donor and phenyl-C_{71}-butyric-acid-methyl ester ($PC_{71}BM$), 3,9-bis(2-methylene-((3-(1,1-dicyanomethylene)-6/7-methyl)-indanone))-5,5,11,11-tetrakis(4-hexylphenyl)-dithieno[2,3-d:2',3'-d']-s-indaceno[1,2-b:5,6-b']dithiophene (ITIC-M) as an acceptor. Based on this hybrid active layer, we manufactured hybrid solar cells and evaluated their characteristics.

CPEs that were introduced into the active layer exhibited hole transport effects without additional introduction of HTLs. Specifically, the PFT-D, the introduced CPEs in the present work, showed work function of 5.10 eV in our previous report that is favorable for hole transport properties. The PFT-D has self-assembled properties due to the difference in dipole between the conjugated backbone and the side chain. The PFT-D that was introduced in the BHJ active layer exhibited the characteristics of its arrangement below the active layer inducing vertical phase separation due to its surface energy properties. This was confirmed by contact angle, X-ray photoelectron spectroscopy (XPS) surface, and depth profiling analyses. Additionally, the morphology and surface potential were formed, which were favorable for charge transport by the introduction of CPEs in the hybrid active layer. This was confirmed by atomic force measurement (AFM) and electrostatic force measurement (EFM) analyses.

The hybrid solar cells introduced in this study can be manufactured more easily than general cells with PEDOT:PSS and have the advantages of excellent performance and stability. Thus, the hybrid cells exhibited PCE of 8.7% in fullerene BHJ with a significant improvement in the J_{SC}, V_{OC}, and FF and presented better stability due to their efficiency reduction rate of 5.74% for 200 h than only BHJ device (with reduction rate of 30.15%) and incorporating PEDOT:PSS device (with reduction rate of 10.84%) in fullerene BHJ device. This strategy applied also in nonfullerene system based on PBDB-T:ITIC-M BHJ exhibited high performance of PCE with 10.8%. This means that these theories can be applied to other systems as well. The simple processed and brilliant efficient hybrid solar cells based on controlling vertical phase separation could be moved up commercialization of OSCs.

2. Results and Discussion

The hybrid solar cells were fabricated in a conventional structure based on a simple one-step coating process of the active

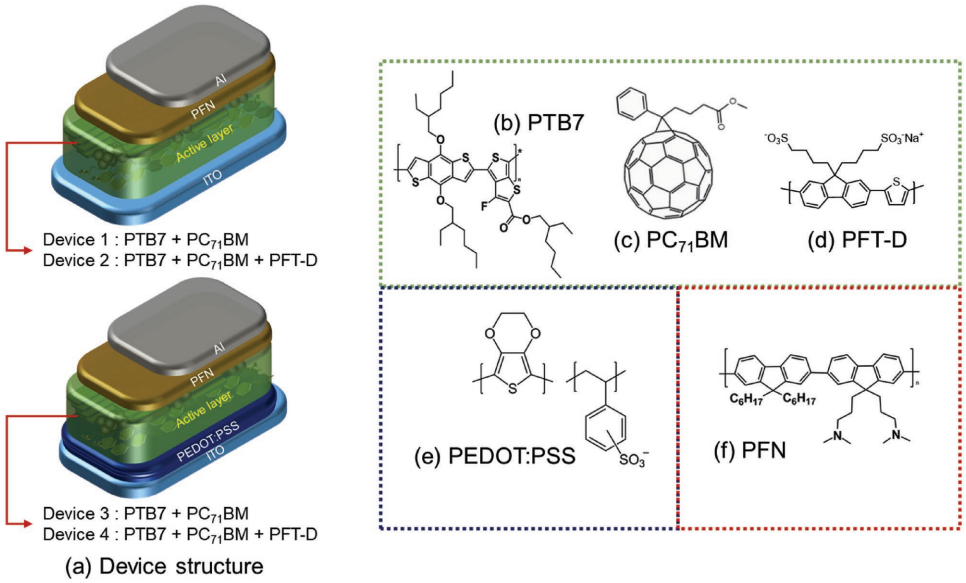

Figure 1. Schematic images of fabricated organic solar cells and their materials structures.

layer by introducing PFT-D into the BHJ that consisted of PTB7 and $PC_{71}BM$. **Figure 1** shows the conventional structure of the organic solar cells used in this study and the structure of the materials introduced into each layer. As shown in Figure 1a, we made four different devices that have different active layer structures of ITO/active layer/PFN/Al in which PEDOT:PSS was not introduced as HTLs and of ITO/PEDOT:PSS/active layer/PFN/Al in which PEDOT:PSS was introduced. The active layer maintains a BHJ structure (Device 1 and Device 3) that is a mixture of PTB7 (Figure 1b) as a donor and $PC_{71}BM$ (Figure 1c) as an acceptor. Additionally, a hybrid BHJ that was added with PFT-D as the CPEs (Figure 1d) into the BHJ, which has self-assembled properties, was formed (Device 2 and Device 4). Figure 1e,f shows the structure of the PEDOT:PSS as HTLs and the structure of PFN as ETLs introduced into the fabricated devices, respectively. Device 1 was constructed only with the BHJ structure without the introduction of the HTLs. Device 2 was manufactured as a BHJ + CPEs with the introduction of the CPEs into BHJ of Device 1. Devices 3 and 4 were made by introducing PEDOT:PSS as HTLs in the structures of Device 1 and Device 2, respectively.

Figure 2 and **Table 1** show the current density–voltage characteristics (Figure 2a), external quantum efficiency (EQE) characteristics (Figure 2b), dark current density–voltage characteristics (Figure 2c), current density–light intensity dependence characteristics (Figure 2d), and photovoltaic characteristics of the fabricated devices. Device 1 exhibited a PCE of 6.3% (J_{SC} = 15.3 mA cm^{-2}, V_{OC} = 0.676 V, and FF = 61.1%). Device 2 exhibited a high PCE of 8.7% (J_{SC} = 16.3 mA cm^{-2}, V_{OC} = 0.737 V, and FF = 72.6%). Devices 3 and 4 exhibited a PCE of 8.3% (J_{SC} = 15.8 mA cm^{-2}, V_{OC} = 0.737 V, and FF = 71.3%) and 8.0% (J_{SC} = 15.6 mA cm^{-2}, V_{OC} = 0.737 V, and FF = 69.6%), respectively. By introducing the PFT-D into the BHJ (Device 2), the PCE was significantly improved from 6.3% to 8.7% because J_{SC} (15.3 mA cm^{-2} → 16.3 mA cm^{-2}), V_{OC} (0.676 V → 0.737 V), and FF (61.1% → 72.6%) were substantially increased. This formed a hybrid BHJ by introducing PFT-D, which was developed as CPEs and showed excellent HTL characteristics in our previous study.[41] The J_{SC}, V_{OC}, and FF performances improved by arranging PFT-D in the interface of the ITO electrode and BHJ.[45] By employing this technique, a high-performance device can be only made with a coating process for the BHJ that does not further incorporate the HTL coating process, and Device 2 (PCE = 8.7%) exhibited superior performance over Device 3 (PCE = 8.3%), which introduced PEDOT:PSS as HTLs. Like PEDOT:PSS that was introduced with a separate coating, this is the result of improving the performance by using PFT-D as HTLs in the interface between the BHJ and ITO in BHJ + CPEs. However, Device 4 exhibited a low performance (PCE = 8.0%) because FF was significantly weakened in comparison with Devices 2 and 3 by the introduction of the BHJ + CPEs on the PEDOT:PSS. This was because the PFT-D played a role as the HTLs in the interface between the BHJ and ITO; however, carrier recombination was increased due to the arrangement of PFT-D between PEDOT:PSS and the BHJ.

As shown in Figure 2b, EQE analysis revealed that the calculated J_{SC} values were 14.57, 15.29, 14.61, and 14.59 mA cm^{-2} for Devices 1–4, respectively. This result showed the highest J_{SC} for Device 2 with the introduction of CPEs, which was consistent with Figure 2 and Table 1. In particular, Device 1 exhibited a lower EQE than Devices 2–4. Additionally, Device 2 exhibited a higher EQE than Devices 1, 3, and 4. The formation of a favorable molecular order in the charge transport within the BHJ can result in high EQE properties.[46,47] Such EQE improvement was possible because the molecular order was favorable for charge transport and a high level of improvement occurred. As a result, Device 2 exhibited the high EQE properties which resulted from the formation of favorable molecular order. As shown in Figure 2c, the dark current density–voltage characteristics revealed the leakage current of fabricated devices. Brabec and co-workers have reported that the higher carrier recombination usually

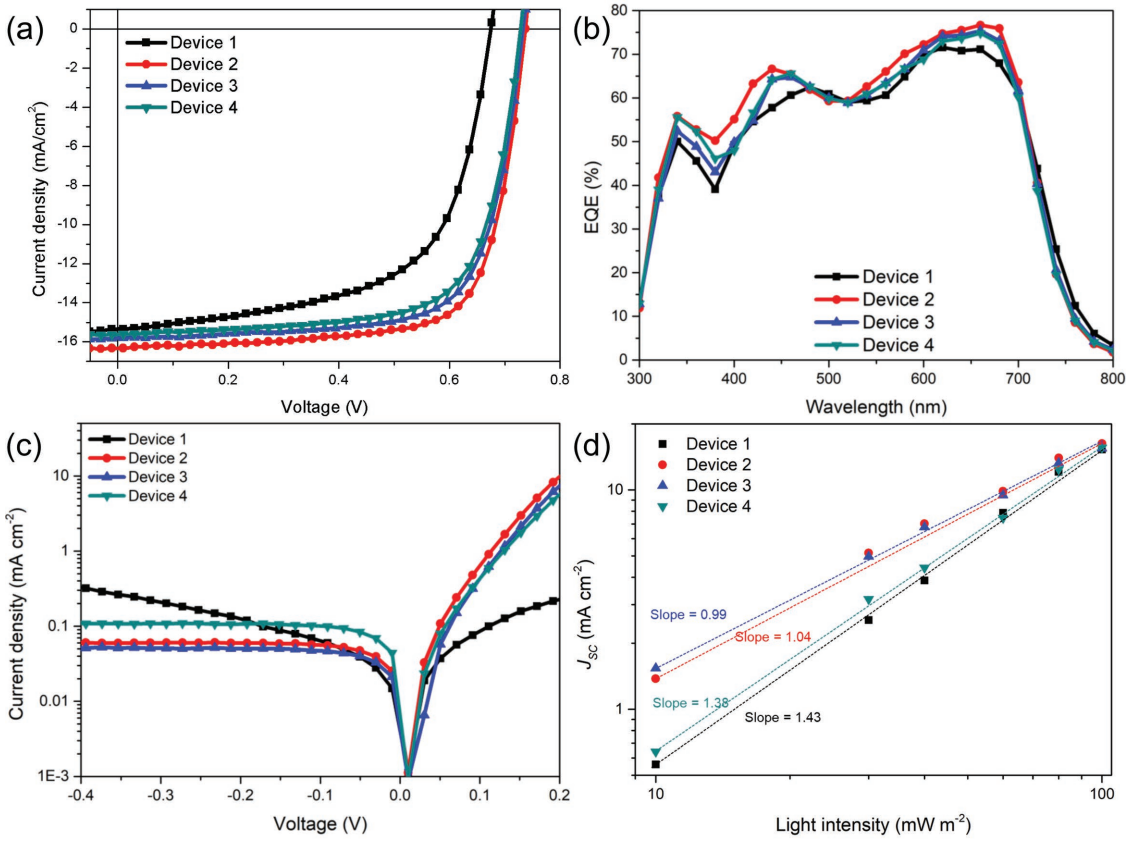

Figure 2. a) Current density–voltage characteristics, b) external quantum efficiency characteristics, c) dark current density–voltage characteristics, and d) current density–light intensity dependence characteristics of fabricated hybrid solar cells.

resulted in lower FF.[48] Devices 1 and 4 showed higher leakage current in revers bias region exhibiting lower FF rather than Devices 2 and 3. Also, Heeger and co-workers have reported the relationship between J_{SC} and light intensity with respect to carrier recombination. The J_{SC} dependence on light intensity measurements provides the tendency of carrier recombination. The linear relationship of J_{SC} and light intensity means the weakness of bimolecular recombination.[49] As shown in Figure 2d, Devices 1–4 exhibited the slope of 1.43, 1.04, 0.99, and 1.38, respectively. As a result, Devices 1 and 4 exhibited low FF properties which resulted from increased carrier recombination. These result is consistent with Table 1 and Figure 2a.

Table 1. Photovoltaic performances of fullerene based BHJ (PTB7: $PC_{71}BM$) + CPEs (PFT-D) hybrid solar cells.

Device structure	J_{SC}[a)] [mA cm^{-2}]	V_{OC}[a)] [V]	FF[a)] [%]	PCE[a)] [%]
Device 1 (BHJ)	15.3 (15.2 ± 0.10)	0.676 (0.67 ± 0.01)	61.1 (61.0 ± 0.09)	6.3 (6.1 ± 0.15)
Device 2 (BHJ + CPEs)	16.3 (16.2 ± 0.10)	0.737 (0.73 ± 0.01)	72.6 (72.1 ± 0.04)	8.7 (8.5 ± 0.18)
Device 3 (PEDOT:PSS/BHJ)	15.5 (15.4 ± 0.08)	0.737 (0.73 ± 0.01)	72.9 (72.5 ± 0.10)	8.3 (8.2 ± 0.18)
Device 4 (PEDOT:PSS/ BHJ + CPEs)	15.6 (15.5 ± 0.11)	0.737 (0.73 ± 0.01)	69.6 (69.4 ± 0.05)	8.0 (7.8 ± 0.17)

[a)]The average values and deviations were obtained from 10 devices.

Figure 3 shows the contact angle and surface energy properties of the formed active layer film. BHJ (Figure 3a), composed of a donor and an acceptor, showed a contact angle of 92.7° and surface energy properties of 16.76 mN m^{-1}. BHJ + CPEs (Figure 3b) showed a contact angle of 103.4° and surface energy properties of 10.89 mN m^{-1}. Additionally, the contact angle and surface properties of PTB7 (Figure 3c), the donor, were 104.8° and 10.23 mN m^{-1}, respectively, and for $PC_{71}BM$ (Figure 3d), the acceptor, they were 60.8° and 40.85 mN m^{-1}, respectively. The PFT-D (Figure 3e) showed a contact angle of 57.6° and surface energy properties of 43.53 mN m^{-1}. The BHJ that consisted of PTB7 and $PC_{71}BM$ showed hydrophobic surface properties, and BHJ + CPEs with PFT-D showed higher hydrophobic surface properties than the BHJ. It was possible to arrange toward ITO (ultraviolet-ozone (UVO) treated, 71.4 mN m^{-1}) which has similar high surface energy properties as PFT-D.[50] This was because PFT-D has the highest surface energy properties among the three components (PTB7, $PC_{71}BM$, and PFT-D) that consist of BHJ + CPEs with its self-assembled properties.[50,51] In general, lower surface energy materials were exposed to the interface of the film and air, and higher surface energy materials were presented in the interface of the film and electrode.[52] Therefore, BHJ + CPEs showed higher hydrophobic

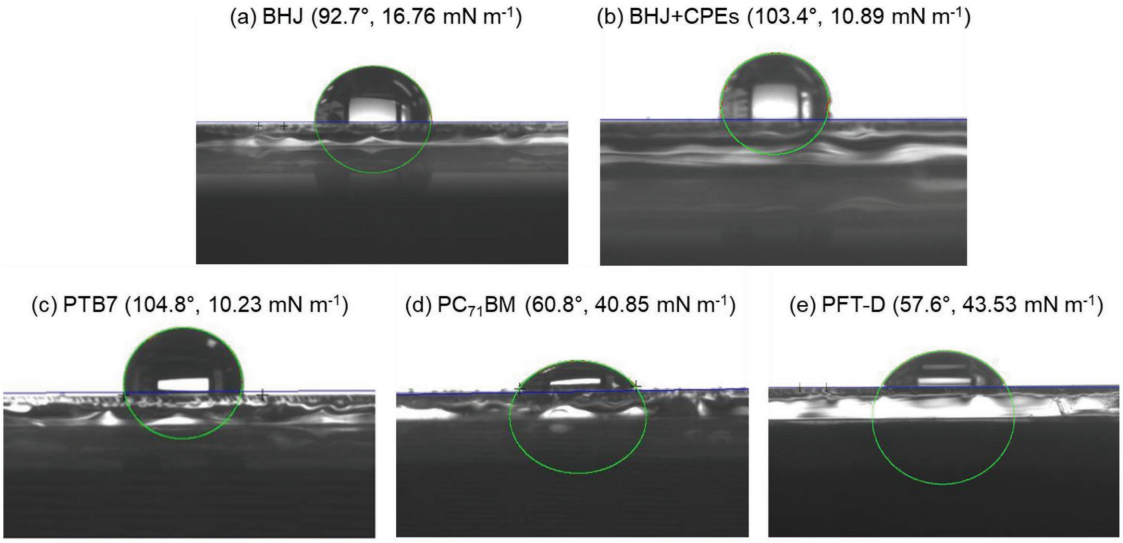

Figure 3. Contact angle characteristics and surface energy characteristics of a) BHJ, b) BHJ + CPEs, c) PTB7, d) $PC_{71}BM$ film, and e) PFT-D.

surface properties compared with BHJ because PTB7 and $PC_{71}BM$, which showed low surface energy properties, were exposed to air in the BHJ with PFT-D.

However, Figure S1 (Supporting Information) shows the surface energy properties of the PEDOT:PSS film and the film with the introduction of the BHJ film on the PEDOT:PSS layer. PEDOT:PSS (in Figure S1a, Supporting Information) and PEDOT:PSS/BHJ in which the BHJ film are deposited on PEDOT:PSS (in Figure S1b, Supporting Information) showed 43.9° and 99.5° contact angles and surface energy properties of 54.63 and 12.87 mN m^{-1}, respectively. The PEDOT:PSS/BHJ structure had higher hydrophobic surface properties (12.87 mN m^{-1}) than the pristine BHJ (16.67 mN m^{-1}). This was because $PC_{71}BM$, which had a relatively high surface energy, was arranged toward the ITO, whereas PTB7, which had a low surface energy, was exposed to air. Furthermore, the PFT-D and PEDOT:PSS had similar surface energy properties resulted in accumulation of PFT-D between BHJ and PEDOT:PSS. This can be explained by a similar tendency of arrangement through the self-assembled properties of PFT-D in BHJ + CPEs.

Figure 4 shows the XPS depth profiling characteristics and ultraviolet photoelectron spectroscopy (UPS) characteristics of BHJ and BHJ + CPEs. We characterized XPS analysis for investigating the vertical phase separation of hybrid active layer by detecting atomic signals.[53] The sample was manufactured in the same manner as the device fabrication process, and the behavior of the CPEs was evaluated for the BHJ (Figure 4a) and for the BHJ + CPEs (Figure 4b). Depth profiling of the manufactured sample was performed by a sputtering process from the top (0 min) to the bottom of the active layer (100 min). The detected signal from the atoms is described as the atomic concentration (%). In Figure 4a, the C_{1S} and O_{1S} signals were high due to PTB7 and $PC_{71}BM$. The F_{1S} and the S_{2P} signals emerged at the beginning but gradually decreased, and the Na_{1S} signal did not appear. This is because, as shown in Figure 3, PTB7, which has low surface energy properties in the BHJ, maintains molecular order at the upper side of the BHJ above the $PC_{71}BM$ distribution.

By contrast, in Figure 4b, similar to Figure 4a, the C_{1s} and O_{1s} signals were high, and the F_{1s} and S_{2p} signals showed a gradual decreasing tendency. The Na_{1s} signal tended to increase at ≈100 min. This occurred due to the Na_{1s} signal that came from PFT-D, which indicated that PFT-D is located at the bottom of the active layer with thickness of ≈10 nm. As shown in Figure 3, PFT-D with a high surface energy in BHJ + CPEs was moved toward the bottom of the active layer in the BHJ, whereas PTB7 and $PC_{71}BM$ with relatively low surface energies were moved toward the top of the active layer. Additionally, unlike Figure 4a, in Figure 4b the signal of C_{1s} tended to increase as it moved toward the bottom of the active layer and then decreased again. This suggests that the molecular order of PTB7/$PC_{71}BM$/PFT-D was formed from the top in the BHJ + CPEs. As a result, in the BHJ + CPEs, the PFT-D was moved toward the ITO by its self-assembled properties and served as HTLs at the interface of ITO and BHJ. Thus, we improved the J_{SC}, V_{OC}, and FF through charge transport and recombination control, which contributed to performance improvement. The results are consistent with Figures 2 and 3 and Table 1.

The UPS characteristics and schematic energy level diagram are shown in Figure 4c,d. The highest occupied molecular orbital (HOMO) level properties of BHJ and BHJ + CPEs hybrid active layer were calculated by UPS measurement.[54,55] The calculated HOMO level of BHJ active layer was 6.16 eV. When the PFT-D was introduced to BHJ active layer, HOMO level shifted slightly up to 5.82 eV. Because of HOMO level shift, the PFT-D doped hybrid active layer (5.82 eV) exhibited decreased energetic barrier between ITO (4.7 eV) and BHJ active layer (6.16 eV) (from 1.46 to 1.12 eV, shown in Figure 4d). This tendency of PFT-D in active layer enhanced internal built-in potential and offered favorable charge transport resulted in increased V_{OC} and FF.

Figure 5 shows the XPS characteristics of the BHJ and BHJ + CPEs. The XPS characteristics were determined by using a monochromatic Al-Kα (1486.6 eV) source. Figure 5a shows the XPS spectra of film surfaces manufactured in the same manner as those for Devices 1–4. No new peaks were formed in all films. Only the intensity of the spectra changed. Figure 5b–f

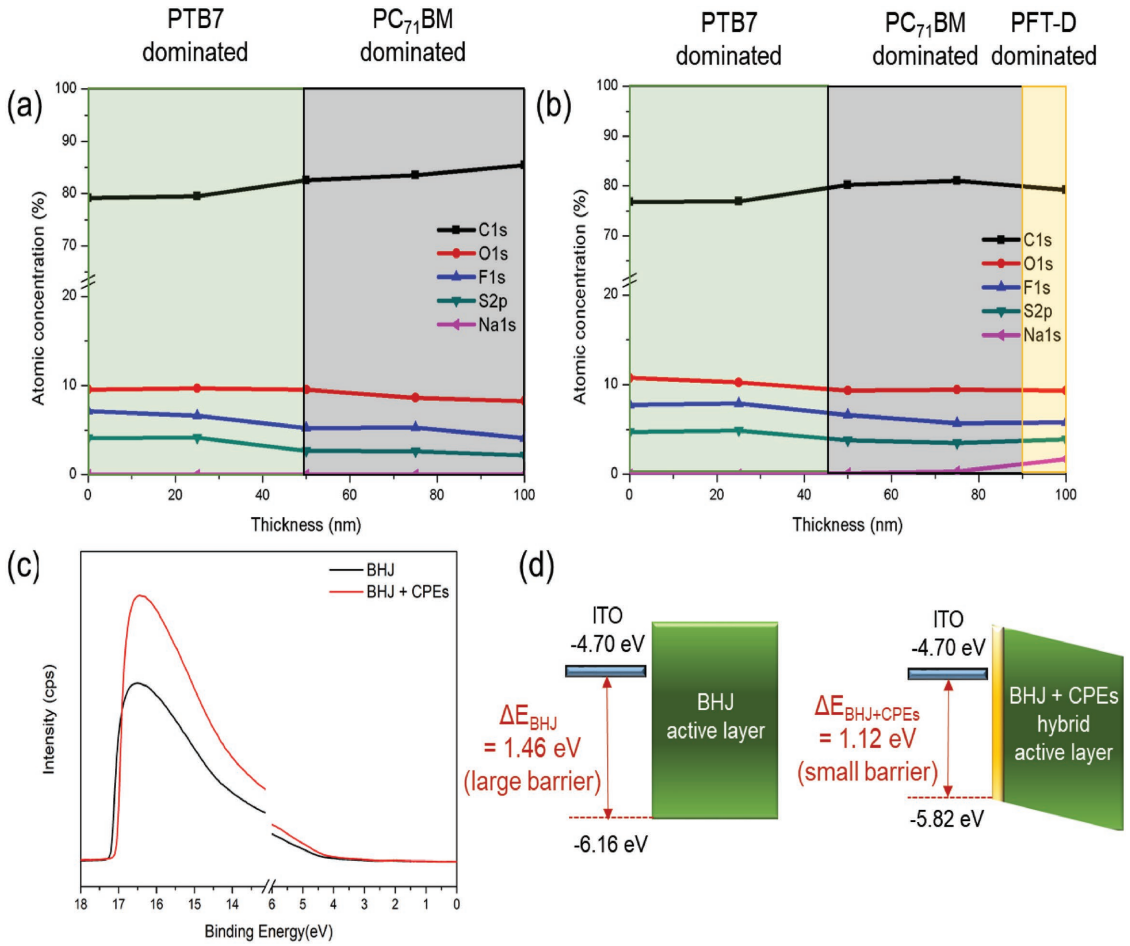

Figure 4. XPS depth-profiling characteristics of a) BHJ active layer and b) BHJ + CPEs hybrid active layer, c) UPS characteristics of BHJ and BHJ + CPEs layer, d) schematic energy level diagram of BHJ and BHJ + CPEs layer.

shows the XPS spectra corresponding to the C_{1s}, O_{1s}, F_{1s}, S_{2p}, and Na_{1s} elements. The main peak for C_{1s} appeared at 284.8 eV (Figure 5b), and the peaks for other elements were compared by using the C_{1s}. The main peak for O_{1s} appeared at 532.5 eV (Figure 5c), which is the binding energy corresponding to organic C=O bonds. The main peak or F_{1s} appeared at 687.2 eV (Figure 5d), which corresponds to organic fluorine units. The main peak for S_{2p} appeared at 163.9 eV (Figure 5e), which corresponds to the S in thiophene. Next, a sub-peak also was present at 165.0 eV, which corresponds to the C—S bonds. Finally, the main peak for Na_{1s} appeared at 1071 eV; however, there were no meaningful peaks to represent the chemical structure (Figure 5f).

The intensity of an atomic signal in the XPS spectra allows analysis of the behavior of materials containing specific atoms.[5,56] The behavior of PTB7, which has a relatively high ratio of F and S atoms, can be analyzed by using the signals from O_{1s}, F_{1s}, and S_{2p}, whereas the behavior of $PC_{71}BM$, which has a relatively high level of C atoms, can be analyzed by using the C_{1s} signal. The behavior of PFT-D in the BHJ can be investigated by the Na_{1s} signal. Figure 5b–e indicated that the introduction of PFT-D in the BHJ reduced the C_{1s} signal and increased the O_{1s}, F_{1s}, and S_{2p} signals. Additionally, as shown in Figure 5f, the Na_{1s} signal was not found for all film surfaces for both BHJ and BHJ + CPEs. This occurred because the introduction of CPEs in the BHJ led to the rearrangement of the internal molecular order. As shown in Figure 4, PFT-D was arranged at the bottom of the active layer, and PTB7 has a molecular order that was arranged at the top of the active layer. Additionally, as shown in Figure 4b, $PC_{71}BM$, which has surface energy properties in the middle between PFT-D and PTB7, showed a molecular order arrangement in the middle area.

However, the XPS spectra of the pristine BHJ and the BHJ + CPEs film revealed a higher intensity than the film with the introduction of PEDOT:PSS. This results suggests that the introduction of PEDOT:PSS changed the molecular order of the BHJ. Specifically, the introduction of PEDOT:PSS significantly reduced the intensity of C_{1s}. Thus, the introduction of PEDOT:PSS, similar to the introduction of PFT-D, controlled the molecular order within the BHJ. $PC_{71}BM$ moved to the bottom of the active layer, and PTB7 moved to the top of the active layer in the molecular order, as PEDOT:PSS reduced the surface energy mismatch between the ITO electrode and the BHJ. This process exhibited favorable properties for charge transport. By contrast, the BHJ + CPEs that was introduced on the PEDOT:PSS showed a similar result, as shown in the

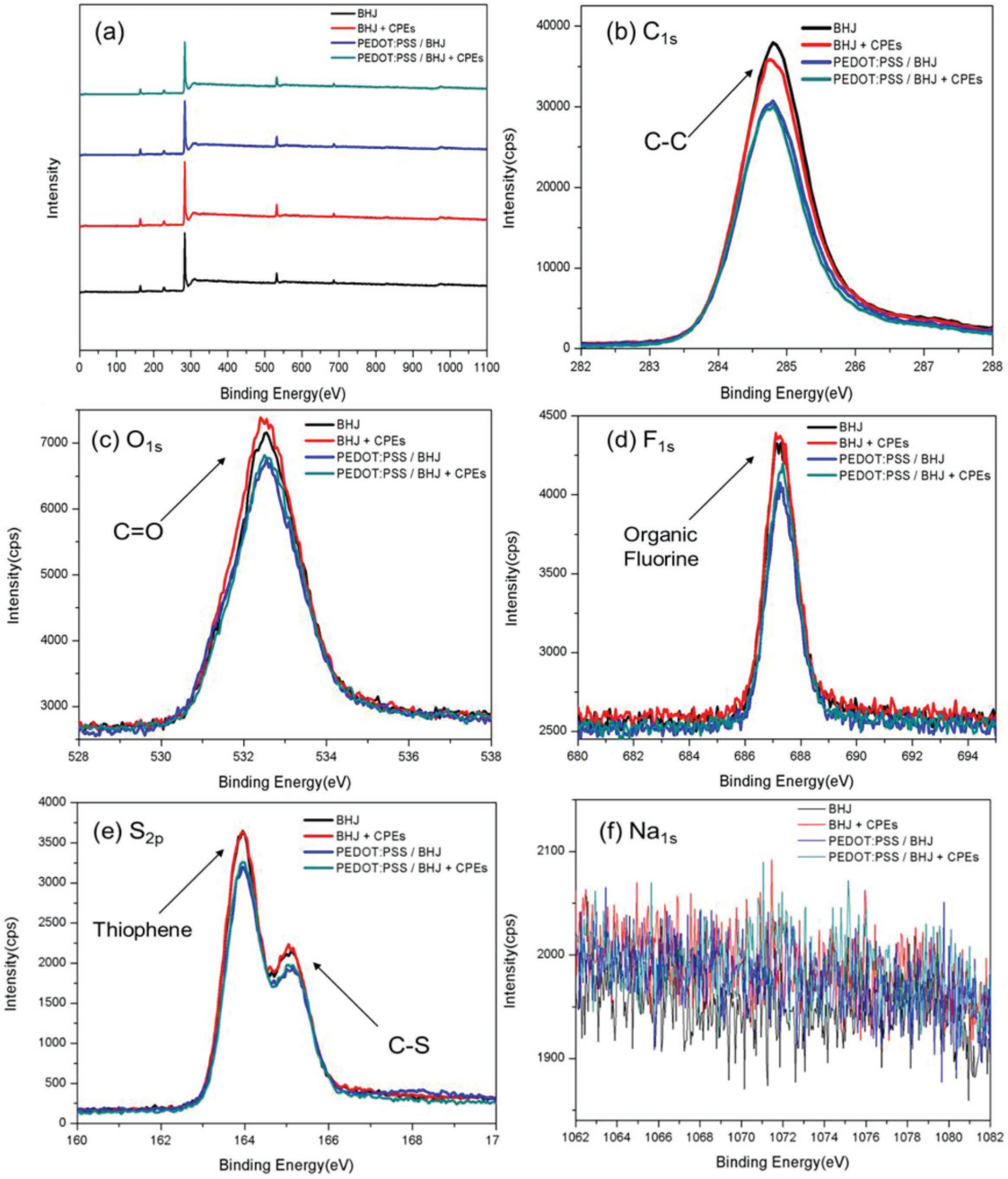

Figure 5. Surface XPS profiling characteristics of a) total survey, b) C_{1s}, c) O_{1s}, d) F_{1s}, e) S_{2p}, and f) Na_{1s} atoms signal.

XPS spectra of the BHJ and BHJ + CPEs mentioned earlier by having slightly lower C_{1s} signals and higher O_{1s}, F_{1s}, and S_{2p} signals than the PEDOT:PSS/BHJ film. As a result, this film showed a rather low performance with a low FF because of the high carrier recombination, although the carrier transport was increased due to the arrangement of the PFT-D in the direction of the PEDOT:PSS.

Figure 6 shows X-ray diffraction (XRD) characterization used to measure the crystalline structure of the hybrid active layer. The figures show the out-of-plane patterns (Figure 6a) and the in-plane pattern (Figure 6b) of pristine BHJ and BHJ + CPEs films. Both pristine BHJ and BHJ + CPEs films showed highly π–π ordered structure indicating high intense (010) peak.[57–59] The XRD pattern of pristine BHJ film showed (010) peak at 2θ = 20.07° in out-of-plane direction and (100) peak at 2θ = 3.20° in in-plane direction. The π–π stacking distance ($d_{\pi-\pi}$) was 0.44 nm and lamellar distance (d_{lamellar}) was 2.76 nm. The XRD pattern of BHJ + CPEs hybrid film showed (010) peak at 2θ = 21.38° in out-of-plane direction and (100) peak at 2θ = 3.18° in in-plane direction. The π–π stacking distance ($d_{\pi-\pi}$) was 0.41 nm and lamellar distance (d_{lamellar}) was 2.77 nm. As a result, the BHJ + CPEs hybrid film formed more highly π–π

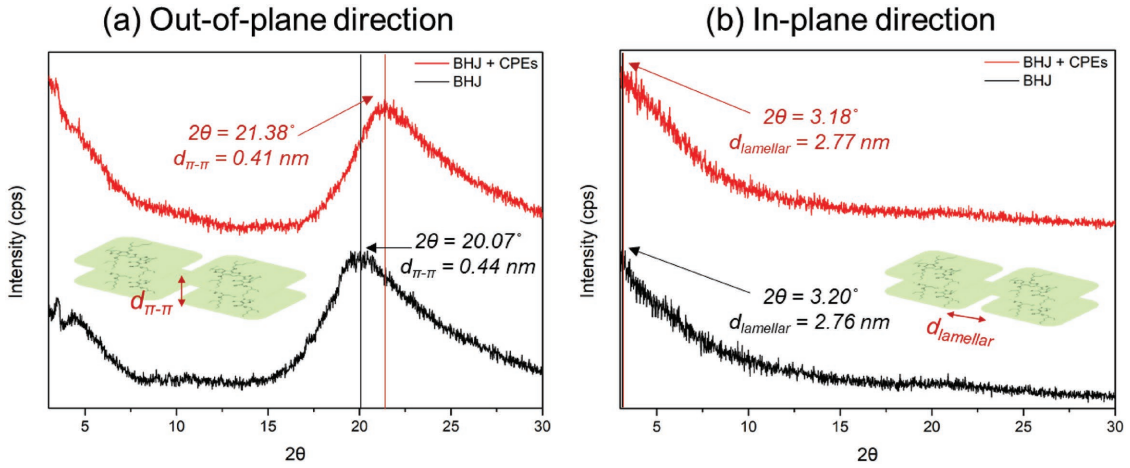

Figure 6. X-ray diffraction characteristics of pristine BHJ and BHJ + CPEs films with respect to a) out-of-plane direction and b) in-plane direction.

ordered structure and closed molecular stacking than pristine BHJ film. With XPS and XRD analyses, the PFT-D introduced in the BHJ induced molecular rearrangement and vertical phase separation that order of PTB7, $PC_{71}BM$, and PFT-D from the top of the BHJ. The ordered structure and closed stacking favored for hole transport properties resulted in enhanced photovoltaic performance.

Scheme 1 shows a molecular order image of the BHJ + CPEs via XPS and XRD analyses. Because of this property, PFT-D showed favorable properties for carrier transport by reducing the surface energy mismatch with the ITO electrode having a role as HTLs in the BHJ. PFT-D incorporated in the BHJ also exhibited excellent J_{SC} and FF characteristics by lowering the carrier recombination. Additionally, PFT-D arranged in the bottom of the BHJ enhanced internal built-in potential resulted in high V_{OC}. This enhancement shows that it is an advantageous method for simplifying the process with a high performance by merely introducing CPEs into the BHJ without an additional coating process for introducing HTLs. These results are consistent with Figures 2–4 and Table 1.

Figure S2a (Supporting Information) shows a schematic image of the post-treatment of the BHJ + CPEs devices fabricated with a conventional structure. Figure S2b–d and Table S1 (Supporting Information) show the surface energy properties, XPS depth profiling analyses, and photovoltaic characteristics according to the post-treatment direction. Device 5 was fabricated by using the opposite direction for post-treatment (downside) during the process of making Device 2 (Figure S2a, Supporting Information). Device 5 showed a PCE of 4.6% (J_{SC} = 15.5 mA cm^{-2}, V_{OC} = 0.676 V, and FF = 44.4%), which was lower than Devices 1 and 2. This low performance of Device 5 was related to the fact that PFT-D did not play the role of HTLs because the orientation of PFT-D in the BHJ became the opposite to that of Device 2. The surface energy properties were increased from 10.89 to 13.90 mN m^{-1} (shown in Figure S2c, Supporting Information) and the Na_{1s} signals were detected at 20–60 nm (shown in Figure S2d, Supporting Information). When the direction of post-treatment changed, the surface properties showed more hydrophilic properties. This tendency was resulted from diffusion of PFT-D from the bottom to the top of the active layer and this diffusion affected by synergistic effects of surface energy and gravity.[60] As a result, the direction of post-treatment changed vertical phase separation of hybrid active layer resulted in decreased photovoltaic performance of Device 5. Thus, the FF was significantly lowered because the carrier recombination increased due to the orientation of PFT-D upon the opposite treatment.

Figure S3a,b and Table S2 (Supporting Information) show the photovoltaic characteristics and dark current density–voltage characteristics of devices fabricated with inverted structures (ITO/ZnO/active layer/MoO_3/Ag). Figure S3c (Supporting Information) shows contact angle and surface energy properties of films coated on ZnO and MoO_3 layer. Figure S3d (Supporting Information) shows dark current density–voltage characteristics. The devices that were introduced only with BHJ or BHJ + CPEs without ETLs of ZnO exhibited a low performance regardless of the introduction of PFT-D. Otherwise, Device 9, which was fabricated with the ZnO as ETLs with the active layer of Device 1, showed a PCE of 8.8% (J_{SC} = 16.4 mA cm^{-2}, V_{OC} = 0.757 V, and FF = 70.6%). Device 10 was fabricated with the incorporation of ZnO with the active layer of Device 2 with structure of ITO/ZnO/PFT-D–BHJ/MoO_3/Ag. Device 10 showed a low PCE of 8.2% (J_{SC} = 16.5 mA cm^{-2}, V_{OC}, = 0.737 V, and FF = 67.3%) because the FF was significantly reduced. Device 11, which was fabricated similarly to the process of Device 10 but with post-treatment on the downside after the introduction of the BHJ + CPEs, showed a PCE of 9.0% (J_{SC} = 17.4 mA cm^{-2}, V_{OC} = 0.737 V, and FF = 69.8%). The high performance of Device 11 was a result of the much improved J_{SC} and FF from Device 10.

As shown in Figure S3c (Supporting Information), The ZnO showed a contact angle of 60.1° and surface energy properties of 40.12 mN m^{-1}. Also, MoO_3 showed a contact angle of 34.2° and surface energy properties of 61.61 mN m^{-1}. In Device 11, the surface energy properties of BHJ + CPEs hybrid active layer were changed. When the direction of post-treatment changed, both BHJ + CPEs hybrid active layer film on ZnO and MoO_3 showed more hydrophilic surface properties. Similar with Device 5, in Device 11, the PFT-D accumulated between BHJ and MoO_3 resulted from synergistic effects of surface energy

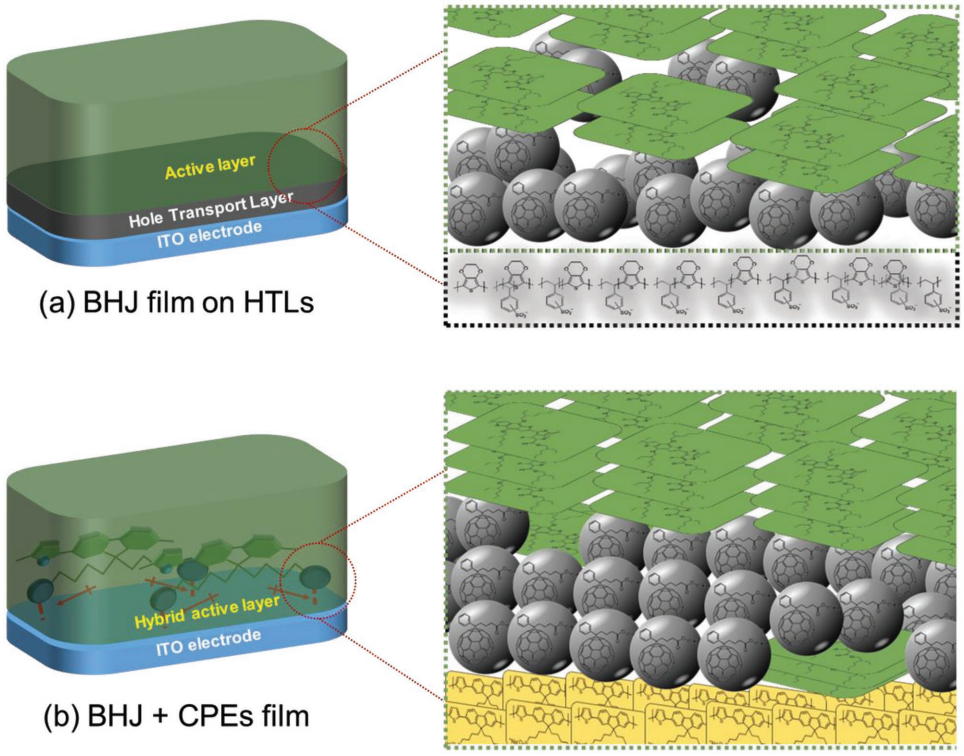

Scheme 1. Schematic image of a) BHJ film on HTLs and b) well-ordered BHJ + CPEs hybrid film.

and gravity.[60] In Device 11, similar with Device 5, the accumulation of PFT-D caused carrier recombination. As shown in Figure S3d (Supporting Information), the dark current density–voltage characteristics of Device 11 showed increased leakage current in reverse bias. This tendency in carrier recombination in Device 11 resulted in low FF. Although the FF of Device 11 was slightly decreased resulted from carrier recombination, the J_{SC} and PCE were higher than Device 9 because of thermodynamic factors following mechanism.

Scheme S1 (Supporting Information) shows the schematic image of thermodynamic film formation with respect to direction of post-treatment. As per the reported results by Chen and co-workers, the decreased surface energy of ITO through surface modification, the amount of polymer donor increases at ITO surface.[61] In our report, both devices fabricated with conventional and inverted structure showed PFT-D accumulated at the bottom of active layer through up side post-treatment (Devices 2 and 10). These tendency resulted from surface energy similarity of PFT-D with ITO and ZnO. Because of PFT-D arranged at the ITO, the surface energy of ITO was decreased by PFT-D. In this formation, most of $PC_{71}BM$ and some PTB7 arranged toward PFT-D. This tendency is consistent with Figure 4b that slightly increased F_{1s} signal at the interface of PFT-D. Then, favorable structure for carrier transport was formed in conventional device (Device 2). Also, not favorable structure for carrier transport was formed in inverted device (Device 10). However, the PFT-D diffused toward top of the active layer through down side treatment forming relative hydrophilic surface resulted from synergistic effects of high surface energy and gravity (Devices 5 and 11). In this formation, most of $PC_{71}BM$ arranged at ITO. Then, favorable structure for carrier transport was formed in inverted device (Device 11). Also, not favorable structure for carrier transport was formed in conventional device (Device 5). These results are well consistent with the Figures 2–4 and Table 1 and Figures S1–S3 and Tables S1 and S2 (Supporting Information).

Figure S4 (Supporting Information) shows the optical characteristics of the BHJ, BHJ + CPEs film, and PFT-D. The BHJ + CPEs films with PFT-D had both higher absorption (Figure S4a, Supporting Information) and emission properties (Figure S4b, Supporting Information) than pristine BHJ film. The optical properties of PFT-D were shown in Figure S4c (Supporting Information). PFT-D was introduced into the BHJ, and then it formed a self-assembled order in the interface between the ITO and BHJ, which controlled the molecular order of the BHJ. Given these properties, the BHJ + CPEs film exhibited higher absorption properties than the pristine BHJ (like EQE in Figure 2b). The PFT-D showed high absorption properties around λ = 300–400 nm and high emission properties around λ = 470–750 nm (shown in Figure S4c, Supporting Information). However, the absorption properties of BHJ + CPEs film were enhanced in entire region. As a result, the enhanced absorption properties of BHJ + CPEs film were resulted from controlling molecular order. Additionally, enhanced absorption properties contributed to the improvement in J_{SC} by forming more carriers and higher emission properties. Then, the enhancemd emission properties of BHJ + CPEs film were resulted from both enhanced absorption properties of BHJ + CPEs film and enhanced emission of PFT-D around λ = 600–700 nm range. As a result, the enhanced absorption

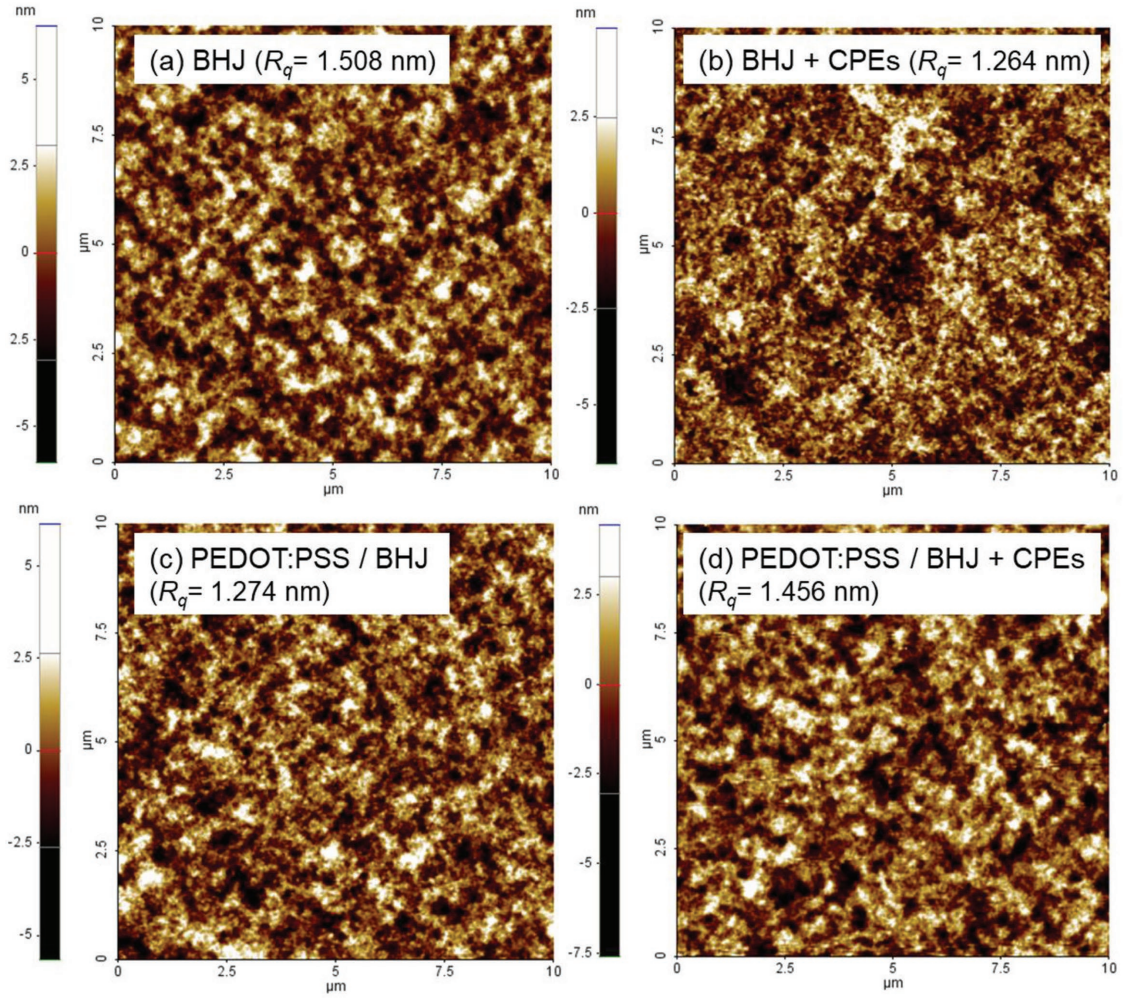

Figure 7. Morphology characteristics of a) BHJ, b) BHJ + CPEs, c) PEDOT:PSS/BHJ, and d) PEDOT:PSS/BHJ + CPEs.

properties and emission properties by introducing PFT-D contributed to high performance of Device 2. These results are consistent with Figures 2–4 and Table 1.

Figure 7 shows the morphology characteristics of a film that has the same structure as the manufactured devices. The film that consisted of only a BHJ (Figure 7a) showed the root mean square (RMS) roughness of 1.508 nm, which indicated a rough morphology. The BHJ was directly introduced on the ITO electrode, and it formed large agglomerates, which revealed a rough morphology due to surface energy mismatch. The film that had PFT-D introduced into the BHJ (Figure 7b), however, showed the RMS roughness of 1.264 nm, which was a relatively fine morphology. This is related to the fact that PFT-D was introduced into the BHJ, as shown in Figures 3 and 4, and was arranged at the bottom of the active layer by the self-assembled properties of PFT-D so that the surface energy mismatches with ITO was reduced. The introduction of PFT-D helped control the molecular order in BHJ, produced a nanostructured morphology, and formed an excellent interpenetrating network for carrier transport. For this reason, Device 2 had higher performance than Device 1 because J_{SC} and FF were significantly improved.

The BHJ film with PEDOT:PSS as HTLs (Figure 7c) had the RMS roughness of 1.274 nm and had a relatively finer morphology than BHJ. This occurred as PEDOT:PSS, which was introduced between the BHJ and the ITO electrode, reduced the surface energy mismatch and formed an excellent morphology for carrier transport. Therefore, J_{SC} and FF were much more improved for Device 3 than for Device 1. However, the BHJ + CPEs film (Figure 7d) with PEDOT:PSS as HTLs had the RMS roughness of 1.456 nm, which indicated a rougher morphology than the BHJ + CPEs without PEDOT:PSS. This is because PFT-D was arranged toward PEDOT:PSS in the BHJ due to its self-assembled property, but this arrangement contributed to the formation of a rough morphology by generating an agglomerate. For this reason, Device 4 exhibited a lower J_{SC} and FF than Device 2. These results are consistent with Figures 2–5 and Table 1.

Figure 8 shows the surface potential characteristics of the film that had the same structure as the fabricated device. The surface potential properties of the pristine BHJ film (Figure 8a) and the BHJ + CPEs film (Figure 8b) were 465.405 mV (R_q = 5.197 mV) and 479.510 mV (R_q = 1.199 mV), respectively. The introduced PFT-D controlled the molecular order in the BHJ while migrating toward the interface between the ITO and BHJ, and it

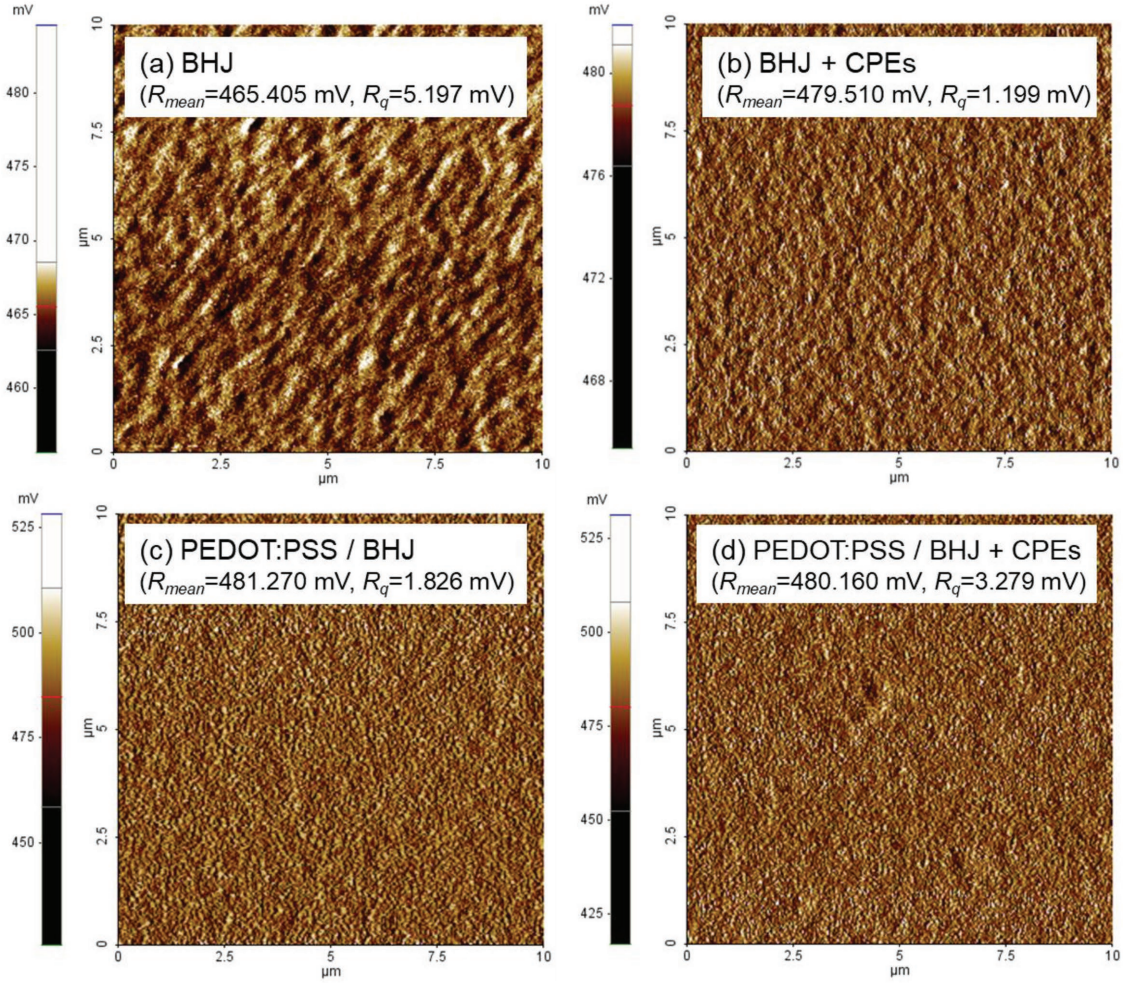

Figure 8. Surface potential characteristics of a) BHJ, b) BHJ + CPEs, c) PEDOT:PSS/BHJ, and d) PEDOT:PSS/BHJ + CPEs.

showed high and uniform surface potential properties. Wu and co-workers reported that they could increase the built-in potential and decrease the carrier recombination by increasing the surface potential in device fabricated with conventional structure. Consequently, they could improve the performance of a device through enhancement of the J_{SC}, V_{OC}, and FF.[62] Additionally, Friedel and co-workers found that the uniform surface potential of HTLs that are introduced into a device fabricated with conventional structure exhibits favorable properties for carrier transport and control carrier recombination.[63] Therefore, the introduction of PFT-D in Device 2 enhanced the J_{SC}, V_{OC}, and FF and improved the built-in potential and charge transport characteristics via producing a high and uniform surface potential.

Figure 8c,d shows surface potential properties of 481.270 mV (R_q = 1.826 mV) for the BHJ film and 480.160 mV (R_q = 3.279 mV) for the BHJ + CPEs film with the introduction of PEDOT:PSS. Both films presented high surface potential properties. Notably, compared to the pristine BHJ, the BHJ film with PEDOT:PSS had a high FF via high and uniform surface potential properties; however, it showed relatively rougher surface potential properties than BHJ + CPEs. Additionally, the surface potential of the BHJ + CPEs film increased with the introduction of PEDOT:PSS but showed rough surface potential properties compared with the BHJ + CPEs film without PEDOT:PSS. This is because the accumulation of PFT-D between BHJ and PEDOT:PSS layer resulted from similar surfae energy. Thus, the aggregation occurred within the interface between PFT-D and PEDOT:PSS, and FF was decreased by increasing the carrier recombination. These results are consistent with Figures 2–7 and Table 1.

Table S3 (Supporting Information) shows the hole mobility properties that were calculated by using the space charge limited current method. The hole mobility was estimated by using the Mott–Gurney equation and by fabricating a hole only device (ITO/active layer/MoO_3/Ag or ITO/PEDOT:PSS/active layer/MoO_3/Ag)[64,65]

$$J = (9/8)\mu\varepsilon_0\varepsilon_r\left(V^2/L^3\right) \quad (1)$$

where μ: Charge carrier mobility,

ε_0: Free-space permittivity,
ε_r: Dielectric constant of the semiconductor,
V: Applied voltage,
L: Thickness of semiconductor layer.

The hole mobilities calculated for the hole-only devices, which were made from the films of Devices 1–4, were

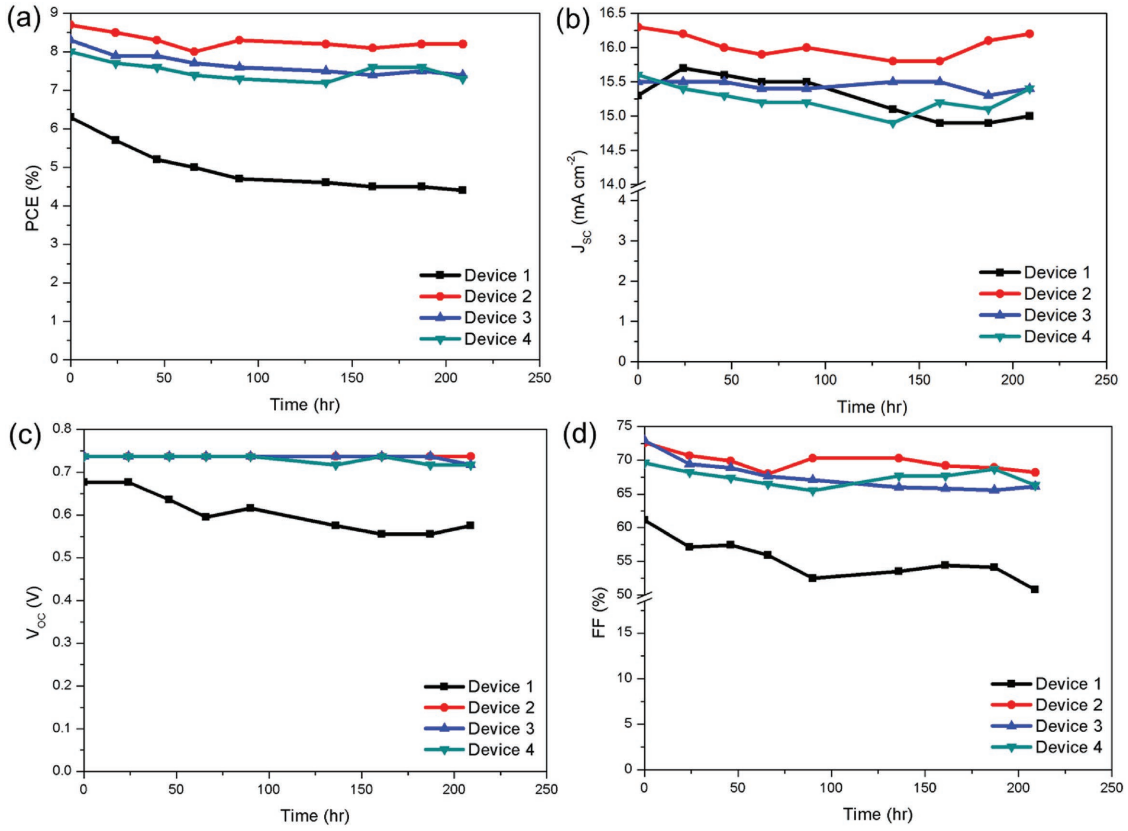

Figure 9. Stability properties of fabricated devices for around 200 h with respect to photovoltaic factors a) PCE, b) J_{SC}, c) V_{OC}, and d) FF.

1.47×10^{-3}, 2.33×10^{-3}, 2.02×10^{-3}, and 1.77×10^{-3} cm^2 V^{-1} s^{-1}, respectively. The BHJ + CPEs film (Device 2) exhibited the highest hole mobility. This was possible by the role of PFT-D as HTLs in the BHJ due to its self-assembled properties, which is consistent with the results in Figures 2–7 and Table 1.

Figure 9 shows the stability properties of the fabricated devices for 200 h. After 200 h, Device 1 showed a PCE of 4.4%, which was 30.15% lower than the initial PCE of 6.3%. Device 2 showed an excellent stability property, indicating a PCE of 8.2%, which was 5.74% lower than the initial PCE of 8.7%. The main factors for the weakening of the performance of Device 1 were related to the reduction of the V_{OC} and FF. This occurred when the surface potential was low, and the carrier recombination increased due to the surface property mismatch between the ITO electrode and the BHJ. By contrast, Device 2 had a higher stability than Devices 1, 3, and 4, which attributed to resolving the surface properties mismatch that originated from the self-assembled properties of PFT-D and to inhibiting the increase in the carrier recombination via the uniform morphology and surface potential. These results are consistent with Figures 2–7 and Table 1.

Figure 10 and **Table 2** show molecular structures of BHJ and photovoltaic properties of PBDB-T:ITIC-M based hybrid solar cells fabricated with PFT-D. The devices with PFT-D showed enhanced photovoltaic performance in the nonfullerene based system same as fullerene based system. The device with pristine BHJ exhibited the PCE of 8.8% (J_{SC} = 17.3 mA cm^{-2}, V_{OC} = 0.798 V, and FF = 63.5%). By introducing the PFT-D into the nonfullerene based BHJ, the PCE was 10.8% (J_{SC} = 17.9 mA cm^{-2}, V_{OC} = 0.919 V, and FF = 65.7%) which is enhanced significantly than pristine BHJ. These results mean that our strategy with CPEs is very impact in both fullerene and nonfullerene based system.

Figure S5 and Table S4 (Supporting Information) show photovoltaic properties of fullerene based hybrid solar cells fabricated with other CPEs series (labeled as PFtT-D, PFbT-D) synthesized in our previous report.[41] The devices with PFtT-D and PFbT-D showed enhanced photovoltaic performance same as PFT-D. The device with PFtT-D and PFbT-D exhibited the PCE of 8.4% (J_{SC} = 15.5 mA cm^{-2}, V_{OC} = 0.737 V, and FF = 73.1%) and 8.3% (J_{SC} = 15.4 mA cm^{-2}, V_{OC} = 0.737 V, and FF = 73.2%), respectively. By introducing the PFtT-D and PFbT-D into the BHJ, the PCE was significantly improved from 6.3% to 8.4% and 8.3% because V_{OC} and FF were substantially increased. This tendency means that the vertical phase separation could be also caused in other CPEs system for favorable enhancing photovoltaic performance. These results suggest that devices fabricated via one-pot coating process could be applied to high performance solar cells industry.

3. Conclusion

Highly efficient and stable OSCs were fabricated through a simple coating process. PFT-D, which can act as HTLs via its

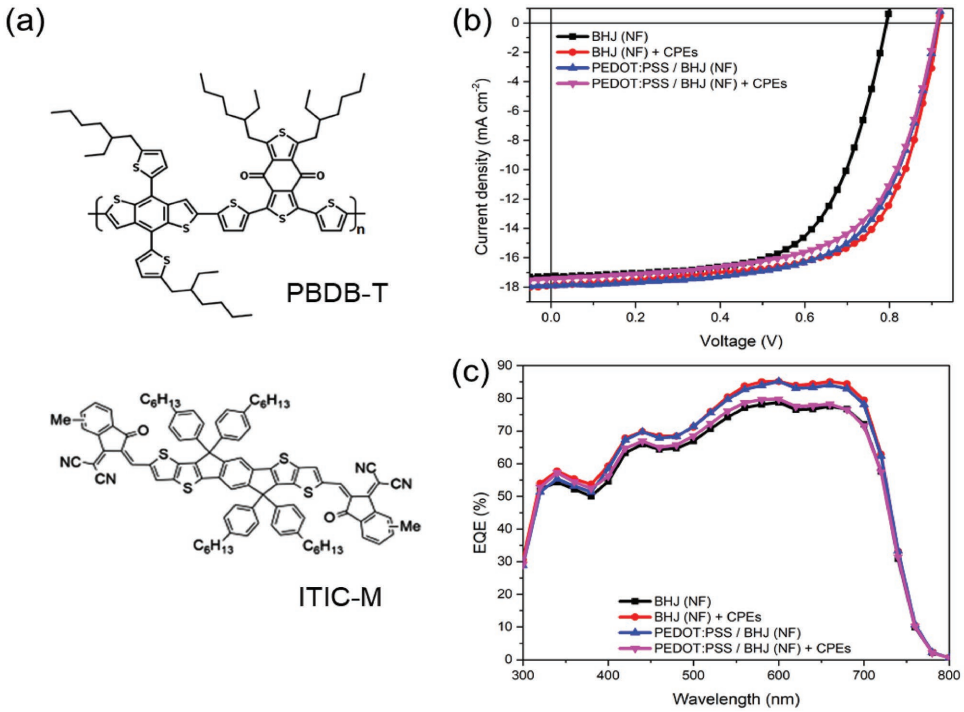

Figure 10. a) Molecular structures of PBDB-T and ITIC-M, b) current density–voltage characteristics, and c) external quantum efficiency characteristics of fabricated PBDB-T:ITIC-M (nonfullerene) based hybrid solar cells.

excellent solubility and dipole properties, was introduced into the BHJ and formed a self-assembled order due to its surface energy properties (Figure 3). PFT-D introduced into the BHJ (with its self-assembled order properties) was arranged in the interface of the ITO electrode and BHJ, and it controlled PTB7 and $PC_{71}BM$ and arranged them at the top and the middle of the BHJ (Figures 4–6), respectively. These properties led to the excellent optical properties within the BHJ and the J_{SC} enhancement through a better carrier generation (Figure S4, Supporting Information). PFT-D formed a uniform and nanostructured morphology due to its characteristics of the arrangement in the BHJ and showed favorable properties for hole transport. Additionally, the introduction of PFT-D produced high surface potential properties and contributed to the improvement of the J_{SC} and FF by controlling the carrier recombination (Figures 2, 7, and 8; Table S3, Supporting Information). As a result, PFT-D, which was introduced into the BHJ, allowed the BHJ components to form a favorable molecular order for hole transport without additional introduction of HTLs. Additionally, PFT-D increased the hole transport and reduced the carrier recombination, which resulted in an improved J_{SC} and FF. With this simple process, we were able to fabricate hybrid OSCs that showed a high PCE of 8.7%, and we were able to make a device with better performance and stability compared with the device that included PEDOT:PSS (8.3%). This strategy to enhancing photovoltaic properties can be also applied to other BHJ and CPE systems. These results of this research have the potential of significantly contributing to the upsizing and commercialization of OSCs.

Table 2. Photovoltaic performances of nonfullerene based BHJ (PBDB-T:ITIC-M) + CPEs (PFT-D) hybrid solar cells.

Device structure	J_{SC}[a)] [mA cm^{-2}]	V_{OC}[a)] [V]	FF[a)] [%]	PCE[a)] [%]
BHJ	17.2 (17.0 ± 0.10)	0.798 (0.79 ± 0.01)	63.5 (63.3 ± 0.07)	8.8 (8.6 ± 0.19)
BHJ + CPEs	17.9 (17.8 ± 0.10)	0.919 (0.91 ± 0.01)	65.7 (65.5 ± 0.05)	10.8 (10.6 ± 0.17)
PEDOT:PSS/BHJ	17.9 (17.8 ± 0.13)	0.919 (0.91 ± 0.01)	63.9 (63.7 ± 0.09)	10.5 (10.3 ± 0.19)
PEDOT:PSS/BHJ + CPEs	17.5 (17.4 ± 0.11)	0.919 (0.91 ± 0.01)	62.7 (62.5 ± 0.10)	10.1 (9.9 ± 0.20)

[a)]The average values and deviations were obtained from 10 devices.

4. Experimental Section

Materials: PTB7 and $PC_{71}BM$ used as donor and acceptor materials for active layer were purchased from 1-Material (Canada). PBDB-T and ITIC-M were purchased from Brilliant Mater (Canada). PFT-D, conjugated polyelectrolytes for self-assembled properties introduced in hybrid active layer, was synthesized as the previous research.[41] ITO glass for fabrication of devices was purchased from AMG (Republic of Korea). PEDOT:PSS introduced as HTLs via additional coating was purchased from Heraeus (Germany). PFN introduced as ETLs was purchased from 1-Material (Canada). Chlorobenzene and 1,8-diiodooctane used as solvent and additives were purchased from Sigma-Aldrich (Germany).

Preparation of Fabrication: To fabrication of hybrid solar cells, the ITO glass was cleaned in order of acetone, Alconox detergent, isopropyl alcohol, and deionized water through

ultrasonication method. The precleaned ITO glass was treated UV-ozone cleaning in UVO cleaner (Ahtech LTS AH 1700) for 15 min. The fullerene based BHJ active layer was formulated with PTB7 and $PC_{71}BM$ with the ratio of 1:1.5 (concentration of 25 mg mL^{-1}) in chlorobenzene (1,8-diiodooctane 3 v/v%). The nonfullerene based BHJ active layer was formulated with PBDB-T and ITIC-M with the ratio of 1:1 (concentration of 20 mg mL^{-1}) in chlorobenzene (1,8-diiodooctane 1 v/v%). Otherwise, the hybrid BHJ active layer was formulated with PFT-D that was synthesized and half time doped (contains of half Na^+ ions) in the previous report with concentration of 1 mg mL^{-1} in the BHJ active layer.[41]

Fabrication of Devices via One-Pot Coating Process: The one-pot coating processed devices fabricated with conventional structure (ITO/BHJ active layer/PFN/Al). The BHJ film was formed onto the UVO-treated ITO glass via spin-coating process of fabricated the BHJ solution with thickness of ≈100 nm. For ETLs, the PFN introduced via spin-coating process is similar with previous report.[2] The metal electrode (Al) was thermal evaporated in the high vacuum chamber (at 1×10^{-7} torr) with rates of 5.0 Å s^{-1} with thickness of ≈100 nm. The active area of fabricated devices was 0.04 cm^{-2}.

Fabrication of Devices with PEDOT:PSS: The devices with PEDOT:PSS layer were fabricated with conventional structure (ITO/PEDOT:PSS/BHJ active layer/PFN/Al). The PEDOT:PSS layer was formed onto the UVO-treated ITO glass via spin-coating process with 4000 rpm and thermal treated at 140 °C on the hot-plate. After introducing HTLs, all fabrication process were same as devices fabricated via one-pot coating process.

Characterization of Fabricated Devices: The characterization of power conversion efficiency and current density–voltage, dark current density–voltage, current density–light intensity dependence properties were measured using Keithley 2400 source meter unit. The light source was solar simulator (Oriel, 100 mW cm^{-2}). The intensity of incident light was measured using reference cell which was calibrated at AM 1.5G. The EQE was measured using incident photon to current efficiency measurement system (Polaronix K3100, Mc science). The contact angle and surface energy properties were measured using contact angle analyzer (DSA100, KRUSS). XPS depth and surface profiling analyses were performed by using ULVAC-PHI 5000 VersaProbe, Phi(Φ). UPS was performed by using AXIS-NOVA, Kratos. The surface morphology and surface potential analyses were performed by using AFM and EFM system (PSIA XE-100). The absorption and emission properties were measured using UV–vis spectrometer (Agilent 8453) and photoluminescence spectrometer (LS55, Perkin Elmer), respectively.

Supporting Information

Supporting Information is available from the Wiley Online Library or from the author.

Acknowledgements

This research was supported by New & Renewable Energy Core Technology Program of the Korea Institute of Energy Technology Evaluation and Planning (KETEP) grant funded by the Ministry of Trade, Industry & Energy (MI, Korea) (Grant no. 20153010140030) and the Human Resources Program in Energy Technology of the Korea Institute of Energy Technology Evaluation and Planning (KETEP), granted financial resource from the Ministry of Trade, Industry & Energy, Republic of Korea. (Grant No. 20174010201540).

Conflict of Interest

The authors declare no conflict of interest.

Keywords

conjugated polyelectrolytes, hole transport layer, organic solar cells, power conversion efficiency, vertical phase separation

Received: September 9, 2018
Revised: October 17, 2018
Published online:

[1] S. J. Jeon, S. J. Nam, Y. W. Han, T. H. Lee, D. K. Moon, *Polym. Chem.* **2017**, *8*, 2979.
[2] Y. W. Han, E. J. Lee, J. Joo, J. Park, T. H. Sung, D. K. Moon, *J. Mater. Chem. A* **2016**, *4*, 10444.
[3] X. Xu, T. Yu, Z. Bi, W. Ma, Y. Li, Q. Peng, *Adv. Mater.* **2018**, *30*, 1.
[4] H. Zhang, H. Yao, J. Hou, J. Zhu, J. Zhang, W. Li, R. Yu, B. Gao, S. Zhang, J. Hou, *Adv. Mater.* **2018**, *30*, 1800613.
[5] P. Cheng, R. Wang, J. Zhu, W. Huang, S. Y. Chang, L. Meng, P. Sun, H. W. Cheng, M. Qin, C. Zhu, X. Zhan, Y. Yang, *Adv. Mater.* **2018**, *30*, 1705243.
[6] B. Kan, Y. Q. Q. Yi, X. Wan, H. Feng, X. Ke, Y. Wang, C. Li, Y. Chen, *Adv. Energy Mater.* **2018**, *8*, 1800424.
[7] Y. Zhang, B. Kan, Y. Sun, Y. Wang, R. Xia, X. Ke, Y. Q. Q. Yi, C. Li, H. L. Yip, X. Wan, Y. Cao, Y. Chen, *Adv. Mater.* **2018**, *30*, 1707508.
[8] X. Che, Y. Li, Y. Qu, S. R. Forrest, *Nat. Energy* **2018**, *3*, 422.
[9] Z. Zheng, Q. Hu, S. Zhang, D. Zhang, J. Wang, S. Xie, R. Wang, Y. Qin, W. Li, L. Hong, N. Liang, F. Liu, Y. Zhang, Z. Wei, Z. Tang, T. P. Russell, J. Hou, H. Zhou, *Adv. Mater.* **2018**, *30*, 1801801.
[10] L. Meng, Y. Zhang, X. Wan, C. Li, X. Zhang, Y. Wang, X. Ke, Z. Xiao, L. Ding, R. Xia, H.-L. Yip, Y. Cao, Y. Chen, *Science* **2018**, *361*, 1094.
[11] J. Nelson, *Mater. Today* **2011**, *14*, 462.
[12] Y. Yi, V. Coropceanu, J.-L. Bredas, *J. Mater. Chem.* **2011**, *21*, 1479.
[13] S. Shoaee, M. Stolterfoht, D. Neher, *Adv. Energy Mater.* **2018**, *8*, 1703355.
[14] S. Liu, P. You, J. Li, J. Li, C.-S. Lee, B. S. Ong, C. Surya, F. Yan, *Energy Environ. Sci.* **2015**, *8*, 1463.
[15] H. Yin, P. Bi, S. H. Cheung, W. L. Cheng, K. L. Chiu, C. H. Y. Ho, H. W. Li, S. W. Tsang, X. Hao, S. K. So, *Sol. RRL* **2018**, *2*, 1700239.
[16] N. D. Eastham, J. L. Logsdon, E. F. Manley, T. J. Aldrich, M. J. Leonardi, G. Wang, N. E. Powers-Riggs, R. M. Young, L. X. Chen, M. R. Wasielewski, F. S. Melkonyan, R. P. H. Chang, T. J. Marks, *Adv. Mater.* **2018**, *30*, 1704263.
[17] S. R. Cowan, A. Roy, A. J. Heeger, *Phys. Rev. B* **2010**, *82*, 245207.
[18] M. Kuik, L. J. A. Koster, G. A. H. Wetzelaer, P. W. M. Blom, *Phys. Rev. Lett.* **2011**, *107*, 1.
[19] N. Gasparini, M. Salvador, T. Heumueller, M. Richter, A. Classen, S. Shrestha, G. J. Matt, S. Holliday, S. Strohm, H. J. Egelhaaf, A. Wadsworth, D. Baran, I. McCulloch, C. J. Brabec, *Adv. Energy Mater.* **2017**, *7*, 1701561.
[20] K. Cho, J. Kim, S. Y. Yoon, K. Y. Ryu, S. R. Jang, B. Lim, K. Kim, *Macromol. Rapid Commun.* **2018**, *39*, 1700630.
[21] K. S. Nalwa, H. K. Kodali, B. Ganapathysubramanian, S. Chaudhary, *Appl. Phys. Lett.* **2011**, *99*, 263301.
[22] H. Yan, J. G. Manion, M. Yuan, F. P. Garcia de Arquer, G. R. McKeown, S. Beaupre, M. Leclerc, E. H. Sargent, D. S. Seferos, *Adv. Mater.* **2016**, *28*, 6491.
[23] T. H. Lai, S. W. Tsang, J. R. Manders, S. Chen, F. So, *Mater. Today* **2013**, *16*, 424.
[24] Z. Yin, J. Wei, Q. Zheng, *Adv. Sci.* **2016**, *3*, 1500362.
[25] R. A. Street, M. Schoendorf, A. Roy, J. H. Lee, *Phys. Rev. B* **2010**, *81*, 205307.
[26] S. Shao, K. Zheng, K. Zidek, P. Chabera, T. Pullerits, F. Zhang, *Sol. Energy Mater. Sol. Cells* **2013**, *118*, 43.

[27] G.-J. A. H. Wetzelaer, M. Kuik, P. W. M. Blom, *Adv. Energy Mater.* **2012**, *2*, 1232.
[28] S. Wheeler, F. Deledalle, N. Tokmoldin, T. Kirchartz, J. Nelson, J. R. Durrant, *Phys. Rev. Appl.* **2015**, *4*, 29.
[29] R. Xu, K. Zhang, X. Liu, Y. Jin, X.-F. Jiang, Q.-H. Xu, F. Huang, Y. Cao, *ACS Appl. Mater. Interfaces* **2018**, *10*, 1939.
[30] B. H. Lee, J.-H. Lee, S. Y. Jeong, S. B. Park, S. H. Lee, K. Lee, *Adv. Energy Mater.* **2015**, *5*, 1401653.
[31] B. Sarkar, M. Jaiswal, D. K. Satapathy, *J. Phys.: Condens. Matter* **2018**, *30*, 225101.
[32] A. Perumal, H. Faber, N. Yaacobi-Gross, P. Pattanasattayavong, C. Burgess, S. Jha, M. A. McLachlan, P. N. Stavrinou, T. D. Anthopoulos, D. D. C. Bradley, *Adv. Mater.* **2015**, *27*, 93.
[33] S. Chen, J. R. Manders, S. W. Tsang, F. So, *J. Mater. Chem.* **2012**, *22*, 24202.
[34] W. Qiu, R. Muller, E. Vorozhazi, B. Conings, R. Carleer, H.-G. Boyen, M. Turbiez, L. Froyen, P. Heremans, A. Hadipour, *ACS Appl. Mater. Interfaces* **2015**, *7*, 3581.
[35] H. Choi, B. Kim, M. J. Ko, D.-K. Lee, H. Kim, S. H. Kim, K. Kim, *Org. Electron.* **2012**, *13*, 959.
[36] H. Yang, C. Gong, G. Hong Guai, C. Ming Li, *Sol. Energy Mater. Sol. Cells* **2012**, *101*, 256.
[37] N. Wijeyasinghe, F. Eisner, L. Tsetseris, Y. Lin, A. Seitkhan, J. Li, F. Yan, O. Solomeshch, N. Tessler, P. Patsalas, T. D. Anthopoulos, *Adv. Funct. Mater.* **2018**, *28*, 1802055.
[38] N. Wijeyasinghe, A. Regoutz, F. Eisner, T. Du, L. Tsetseris, Y. H. Lin, H. Faber, P. Pattanasattayavong, J. Li, F. Yan, M. A. McLachlan, D. J. Payne, M. Heeney, T. D. Anthopoulos, *Adv. Funct. Mater.* **2017**, *27*, 1701818.
[39] H. Zhou, Y. Zhang, C.-K. Mai, S. D. Collins, T.-Q. Nguyen, G. C. Bazan, A. J. Heeger, *Adv. Mater.* **2014**, *26*, 780.
[40] H. Xu, X. Fu, X. Cheng, L. Huang, D. Zhou, L. Chen, Y. Chen, *J. Mater. Chem. A* **2017**, *5*, 14689.
[41] E. J. Lee, M. H. Choi, Y. W. Han, D. K. Moon, *ACS Appl. Mater. Interfaces* **2017**, *9*, 44060.
[42] Y. Gui, C. Jia, J. Zhou, Q. Kang, H. Yao, L. Lu, B. Xu, J. Hou, *Chem. Mater.* **2018**, *30*, 6005.
[43] W. Cai, C. Musumeci, F. N. Ajjan, Q. Bao, Z. Ma, Z. Tang, O. Inganas, *J. Mater. Chem. A* **2016**, *4*, 15670.
[44] P. Bi, T. Xiao, X. Yang, M. Niu, Z. Wen, K. Zhang, W. Qin, S. K. So, G. Lu, X. Hao, H. Liu, *Nano Energy* **2018**, *46*, 81.
[45] H. Kang, J. Lee, S. Jung, K. Yu, S. Kwon, S. Hong, S. Kee, S. Lee, D. Kim, K. Lee, *Nanoscale* **2013**, *5*, 11587.
[46] X. Xu, Z. Li, Z. Bi, T. Yu, W. Ma, K. Feng, Y. Li, Q. Peng, *Adv. Mater.* **2018**, *1800737*, 1.
[47] H. Hu, K. Jiang, P. C. Y. Chow, L. Ye, G. Zhang, Z. Li, J. H. Carpenter, H. Ade, H. Yan, *Adv. Energy Mater.* **2018**, *8*, 1.
[48] N. Gasparini, X. Jiao, T. Heumueller, D. Baran, G. J. Matt, S. Fladischer, E. Spiecker, H. Ade, C. J. Brabec, T. Ameri, *Nat. Energy* **2016**, *1*, 16118.
[49] H. Choi, S. Ko, T. Kim, P.-O. Morin, B. Walker, B. H. Lee, M. Leclerc, J. Y. Kim, A. J. Heeger, *Adv. Mater.* **2015**, *27*, 3318.
[50] Z. Zhong, Y. Zhong, C. Liu, S. Yin, W. Zhang, D. Shi, *Phys. Status Solidi A* **2003**, *198*, 197.
[51] A. Garcia, G. C. Welch, E. L. Ratcliff, D. S. Ginley, G. C. Bazan, D. C. Olson, *Adv. Mater.* **2012**, *24*, 5368.
[52] S. Honda, H. Ohkita, H. Benten, S. Ito, *Adv. Energy Mater.* **2011**, *1*, 588.
[53] W. L. Xu, B. Wu, F. Zheng, H. Bin Wang, Y. Z. Wang, F. G. Bian, X. T. Hao, F. Zhu, *Org. Electron. Phys., Mater. Appl.* **2015**, *25*, 266.
[54] J. W. Jo, J. W. Jung, S. Bae, M. J. Ko, H. Kim, W. H. Jo, A. K. Y. Jen, H. J. Son, *Adv. Mater. Interfaces* **2016**, *3*, 1500703.
[55] S. Braun, W. R. Salaneck, M. Fahlman, *Adv. Mater.* **2009**, *21*, 1450.
[56] Y. Busby, E. J. W. List-Kratochvil, J.-J. Pireaux, *ACS Appl. Mater. Interfaces* **2017**, *9*, 3842.
[57] Y. Zheng, T. Goh, P. Fan, W. Shi, J. Yu, A. D. Taylor, *ACS Appl. Mater. Interfaces* **2016**, *8*, 15724.
[58] X. Long, N. Wang, Z. Ding, C. Dou, J. Liu, L. Wang, *J. Mater. Chem. C* **2016**, *4*, 9961.
[59] Y. Jang, Y. Ju Cho, M. Kim, J. Seok, H. Ahn, K. Kim, *Sci. Rep.* **2017**, *7*, 1.
[60] Q. Sun, F. Zhang, Q. An, M. Zhang, X. Ma, J. Zhang, *ACS Appl. Mater. Interfaces* **2017**, *9*, 8863.
[61] L. Huang, G. Wang, W. Zhou, B. Fu, X. Cheng, L. Zhang, Z. Yuan, S. Xiong, L. Zhang, Y. Xie, A. Zhang, Y. Zhang, W. Ma, W. Li, Y. Zhou, E. Reichmanis, Y. Chen, *ACS Nano* **2018**, *12*, 4440.
[62] Z. He, C. Zhong, X. Huang, W. Y. Wong, H. Wu, L. Chen, S. Su, Y. Cao, *Adv. Mater.* **2011**, *23*, 4636.
[63] H.-T. Chien, M. Polzl, G. Koller, S. Challinger, C. Fairbairn, I. Baikie, M. Kratzer, C. Teichert, B. Friedel, *Surf. Interfaces* **2017**, *6*, 72.
[64] F. MacHui, S. Rathgeber, N. Li, T. Ameri, C. J. Brabec, *J. Mater. Chem.* **2012**, *22*, 15570.
[65] L. Li, H. Lin, X. Kong, X. Du, X. Chen, L. Zhou, S. Tao, C. Zheng, X. Zhang, *Nanoscale* **2018**, *10*, 9971.

